Biosensors and Bioelectronics 182 (2021) 113171

Contents lists available at ScienceDirect

Biosensors and Bioelectronics

journal homepage: http://www.elsevier.com/locate/bios

DNA walker-assisted aptasensor for highly sensitive determination of *Ochratoxin A*

Yahui Wang [b,1], Wei Song [a,1], Haiyan Zhao [b], Xin Ma [a], Shuying Yang [a], Xiujuan Qiao [b], Qinglin Sheng [a,b,*], Tianli Yue [a,**]

[a] College of Food Science and Technology, Northwest University, Laboratory of Nutritional and Healthy Food-Individuation Manufacturing Engineering/Research Center of Food Safety Risk Assessment and Control, Xi'an, Shaanxi, 710069, China
[b] College of Chemistry & Materials Science/Key Laboratory of Synthetic and Natural Functional Molecule Chemistry of Ministry of Education/Shaanxi Provincial Key Laboratory of Electroanalytical Chemistry, Northwest University, Xi'an, Shaanxi, 710069, China

ARTICLE INFO

Keywords:
Aptasensor
Signal amplification
DNA walker
MoOx
Ochratoxin A

ABSTRACT

Ochratoxin A (OTA), a toxic secondary metabolite produced via various fungus, poses a serious threat to the health of human beings and animals. In this paper, an aptasensor for OTA detection based on gold nanoparticles decorated molybdenum oxide (AuNPs-MoO_x) nanocomposites, hybridization chain reaction (HCR) and a restriction endonuclease (Nb.BbvCI)-aided walker DNA machine was successfully constructed. In this electrochemical platform, the HCR was also used to embed more electrical signal molecules of methylene blue (MB) on silver nanoparticles (AgNPs) to achieve signal amplification. Under the optimum conditions, after adding OTA and Nb.BbvCI in turn and responding adequately under appropriate conditions, aptamer-DNA (6-DNA) carries the OTA away from the electrode surface, and walker DNA was hybridized autonomously with 5-DNA, releasing a large amount of 5′-DNA with the help of Nb.BBVCI. Finally, the electrochemical signal obtained by differential pulse voltammetry (DPV) was weakened. As an artificial and popular signal amplification technique, the DNA walking machine greatly improved the sensitivity. The proposed biosensor exhibited excellent analytical performance in the range of 0.01–10000 pg mL^{-1} with a detection limit as low as 3.3 fg mL^{-1}. Furthermore, direct comparison with ultraperformance liquid chromatography (UPLC) indicates excellent agreement to actual samples such as apple juice, orange juice, red wine and serum.

1. Introduction

Ochratoxin A is a secondary metabolite generated by various funguses such as aspergillus and penicillium, which is high contaminated in food and animal feed with hepatotoxicity, carcinogenicity, nephrotoxicity, and other toxic effects, causing various degrees of damage to human and animal bodies (Zhang et al. 2018, 2019). The European Commission has specified the maximum permitted levels of OTA in different food in 2 ng g^{-1} in wine, 3 ng g^{-1} in processed cereal products and 5 ng g^{-1} in raw cereal grains (Quintela et al., 2013). Currently, OTA testing still needs to be improved in terms of selectivity and quick access to results. Therefore, an accurate, sensitive, efficient, and convenient method for determining the presence of OTA is of great significance in monitoring its co-contamination. Nowadays, researchers have made a great contribution in OTA detection, such as electrochemiluminescent immunoassay (Lv et al., 2015), immunochromatographic assay (Yan et al., 2020), chemiluminescent immunoassay (Freitas et al., 2019) and fluorescence sensor (Hao et al., 2020). Nevertheless, most of the sensors are time-consuming and depend on expensive equipment, skilled technicians, and complicated pretreatment procedures, which are not suitable as point-of-care diagnostic devices for mycotoxin field application.

Electrochemical sensors have become one of the most predominant point-of-care diagnostic tools in recent years because of their simplicity, rapidity, and low cost. Signal amplification strategy is a key component of molecular detection and useful to enhance the sensitivity of the sensing system (Tao et al., 2018). So far, polymerase chain reaction,

* Corresponding author. College of Food Science and Technology, Northwest University, Laboratory of Nutritional and Healthy Food-Individuation Manufacturing Engineering/Research Center of Food Safety Risk Assessment and Control, Xi'an, Shaanxi, 710069, China.
** Corresponding author.
E-mail address: qlsheng@nwu.edu.cn (Q. Sheng).
[1] Authors contributed equally to this work.

https://doi.org/10.1016/j.bios.2021.113171
Received 2 February 2021; Received in revised form 3 March 2021; Accepted 13 March 2021
Available online 18 March 2021

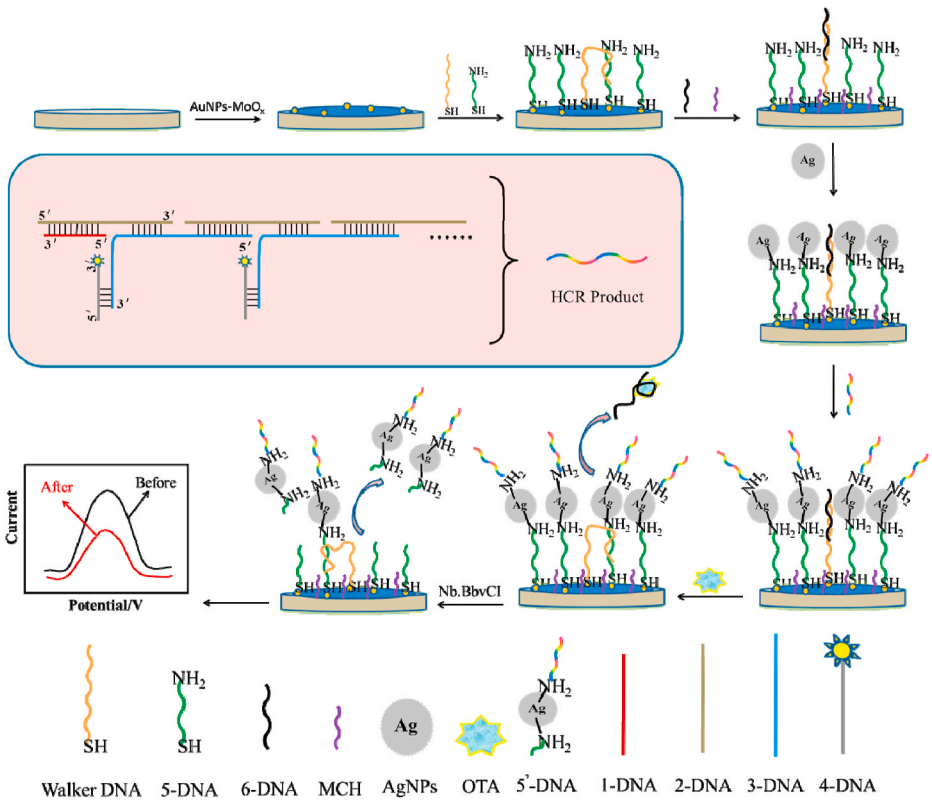

Scheme 1. Illustration of the HCR and walker DNA-assisted electrochemical aptasensor.

enzyme assisted cycle, rolling circle amplification, toehold-mediated strand displacement amplification and DNA machines are used to improve the sensitivity of analysis methods (Wei et al., 2019; Wang et al., 2018; Shu et al., 2017a). These amplification technologies other than DNA machines are limited due to strict experimental conditions and complicated operations (Wei et al., 2019). Moreover, DNA has been widely used to design various DNA-based machines including "DNA nippers", "DNA motors", "DNA robots", "DNA tweezers", "DNA rollers" and "DNA walkers" due to its advantages of diversity, predictability, and exquisite specificity (Yang et al., 2019; Chang et al., 2019). Thereinto, DNA walker has gained tremendous attention from analytical communities for the detection of proteins, cells and nucleic acids due to their outstanding locomotion and controllability. Recently, a new protein binding-induced proximity recognition and polymerase-powered DNA walker strategy has been designed for electrochemical protein analysis (Chen et al., 2019). An enzyme-free and isothermal fluorescence sensor based on dual-3D DNA walker has been fabricated for ultrasensitive detection of telomerase activity with a detection limit as low as 7 cells mL^{-1} (Shen et al., 2021). Additionally, a superwettable biosensor based on a dual-DNA walker strategy has been developed for detection of foodborne microorganisms single stranded DNA in microdroplets (Zhang et al., 2020).

The sensitivity of sensor platform to realize molecular detection is not only related to the design of signal amplification strategy, but also to the performance of electrode materials. Molybdenum oxide (MoO_x), a kind of typical transition metal oxide nanomaterials, has attracted significant attention due to their excellent properties including rich redox activities, good hole extraction properties, low cost, pH neutral, nontoxic and environmental friendliness (Sari and Ting 2018; Kang et al., 2018). It owns multiple phases ranging from stoichiometric molybdenum oxide (MoO_3) to fully reduced molybdenum oxide (MoO_2) with several intermediate phases. As the degree of reduction increases, the color of the solution changes from yellow, light blue to dark blue, and at the same time the Mo^{6+} are reduced to Mo^{5+} and Mo^{4+} (Hu et al., 2012; Li et al., 2017; Zhan et al., 2018). MoO_x has been widely used in the field of catalyst (Haber and Lalik 1997), bioimaging (Veerapandian et al., 2017), biosensing (Dhenadhayalan et al., 2017), cancer therapy (Yin et al., 2018), excellent field emitters (Zhou et al., 2018) and electrochemical capacitor (Yao et al., 2016) due to the following advantages: (1) MoO_x can be completely degraded into the trace element Mo that is necessary for human tissues under the pH dependent oxidation condition, which is harmless to human body and can be used for cancer treatment (Yin et al., 2018; Song et al., 2016); (2) MoO_x has both oxidizability and reducibility due to the existence of the various oxygen-vacancies structures, which leads to extensive research of MoO_x as an electrode material (Guo et al., 2019). Undoubtedly, the combination of DNA Walker and MoO_x nanomaterials greatly improves the sensitivity of electrochemical sensor.

To detect food contaminated with OTA, it is critical to develop molecular tools which is capable of tuning the sensitivity and specificity of DNA walkers for bioanalysis. Therefore, the development of an OTA aptasensor that takes advantages of AuNPs-MoO_x nanocomposites, HCR and Nb.BbvCI-aided DNA walker machine is presented. DPV is used to determinate OTA in apple juice, orange juice and red wine. The aptasensor exhibits a wide linear range of 0.01–10000 pg·$mL^{-1}$and a low detection limit of 3.3 fg mL^{-1} for electrochemical detection of OTA. Moreover, the system showed good selectivity, repeatability and stability.

2. Results and discussion

2.1. Principle of the electrochemical aptasensor for OTA

As shown in Scheme 1, the electrochemical sensing principle is achieved through two signal amplification strategies, HCR and walker DNA. During the process of HCR: (1) A mixture of two DNA (2-DNA and 3-DNA) is stable in the absence of initiator DNA (1-DNA); (2) The added initiator could bind to 2-DNA after hybridization between

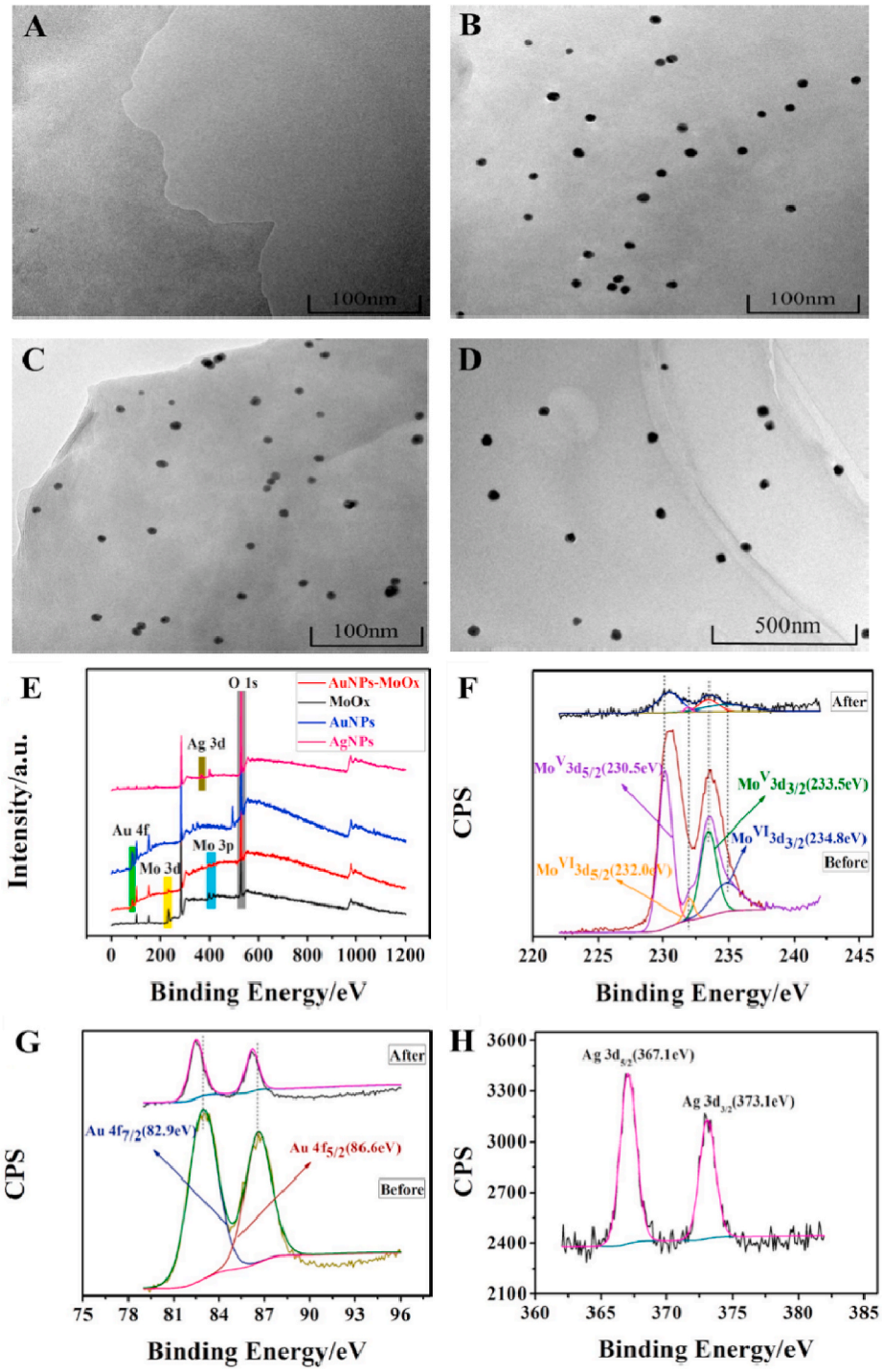

Fig. 1. TEM images of (A) MoO_x, (B) AuNPs, (C) AuNPs-MoO_x and (D) AgNPs. The full XPS spectra of (A) MoO_x, AuNPs, AuNPs-MoO_x and AgNPs; and the corresponding high resolutions of (B) Mo, (C) Au, and (D) Ag elements.

complementary regions, exposing a single-stranded region which is able to combine 3-DNA; (3) As a result, another single-stranded region belonging to 3-DNA is generated, where one partial sequence is identical to the original initiator and triggers more reactions, and others could hybridize with MB labeled 4-DNA; (4) Each initiator could propagate a hybridization events between alternate DNA (2-DNA and 3-DNA) to form a nicked dsDNA with repeating units. The number of HCR product carrying MB continues to increase until the DNA (2-DNA and 3-DNA) supply is exhausted. To realize the combination of the aptamer chains and glassy carbon electrode (GCE), AuNPs-MoO_x nanocomposites were synthesized and used. In general, walker DNA and 5-DNA were immobilized on the surface of MoOx-Au nanocomposites via gold-sulfur self-assembly (Hu et al., 2019). In this situation, the base sequence of 5-DNA was partially complementary to the base sequence of walker DNA. OTA-aptamer (6-DNA) with more binding sites could replace 5-DNA to hybridize with walker DNA. AgNPs can indirectly bind HCR product to 5-DNA by the complexation of Ag–NH_2. Once OTA exists, 6-DNA is detached from the electrode surface to capture targets specifically, resulting in a combination between walker DNA and 5-DNA. In the presence of restriction endonuclease (Nb.BbvCI), the part base sequence of 5-DNA near the 3′ ends is cut off, which cause partial 5-DNA/AgNPs/HCR product (5′-DNA) to fall away from the electrode

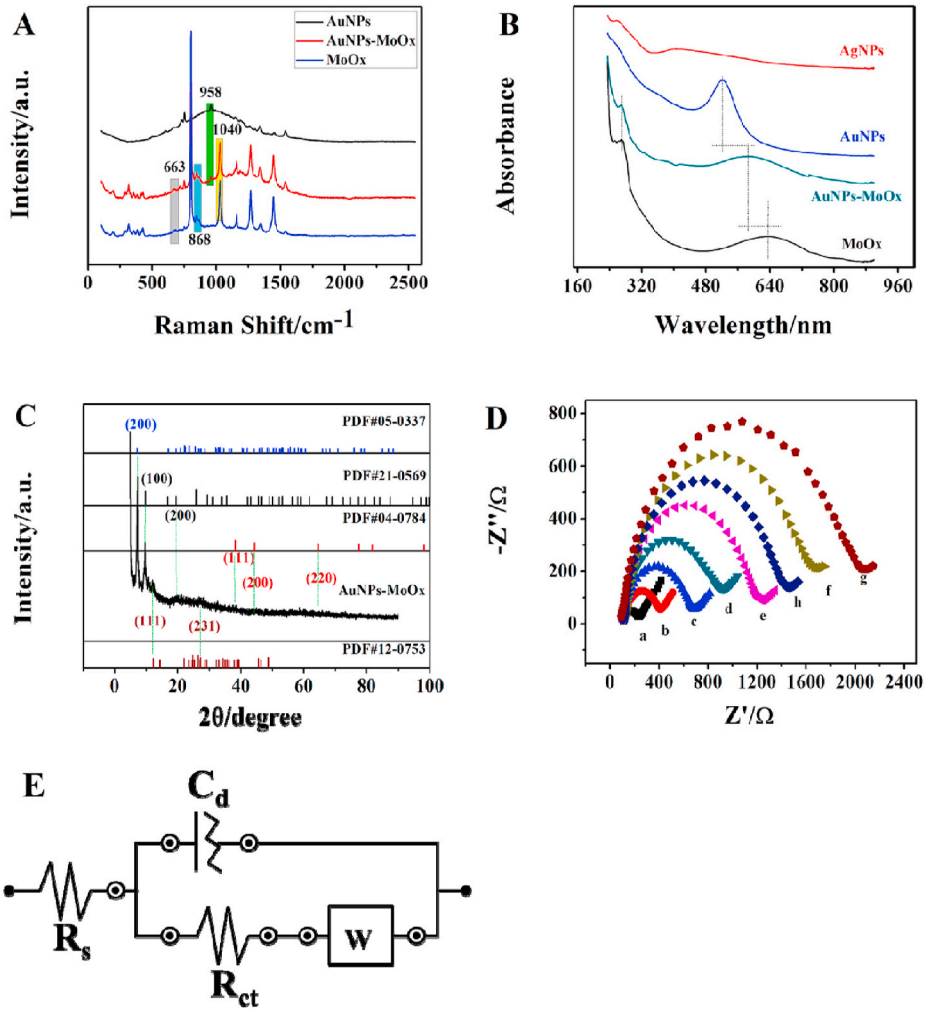

Fig. 2. (A) Characteristic Raman spectra of AuNPs, MoO_x and AuNPs-MoO_x with 632.8 nm excitation; (B) The UV–vis spectrum of AuNPs, MoO_x, AuNPs-MoO_x and AgNPs; (C) XRD pattern of AuNPs-MoO_x nanocomposites; (D) Nyquist plots for the aptasensor obtained after each fabrication step recorded in 5 mM $[Fe(CN)_6]^{3-/4-}$ in 0.1 M KCl solutions, under open circuit potential of 0.27 V *vs.* Ag/AgCl electrode in a frequency range of 100 kHz to 0.1 Hz: (a) GCE, (b) AuNPs-MoO_x/GCE, (c) walker DNA&5-DNA/AuNPs-MoO_x/GCE, (d) MCH/walker DNA&5-DNA/AuNPs-MoO_x/GCE, (e) aptamer-OTA-&AgNPs/MCH/walker DNA &5-DNA/AuNPs-MoO_x/GCE, (f) 1-DNA/aptamer-OTA&AgNPs/MCH/walker DNA&5-DNA/AuNPs-MoO_x/GCE, (g) 2-DNA&3-DNA&4-DNA/1-DNA/aptamer-OTA-&AgNPs/MCH/walker DNA&5-DNA/AuNPs-MoO_x/GCE, and (h) OTA&Nb.BbvCI interaction with the modified electrode; (E) The model circuit of EIS including R_{ct}, Z_w, solution resistance (R_s) and double-layer capacitance (C_d).

and weak the electrochemical signal. Therefore, the quantitative detection of OTA is achieved.

2.2. Characterization of the MoOx nanosheets, AuNPs, AuNPs-MoOx nanocomposites and AgNPs

Transmission electron microscope (TEM) was used to characterize the morphologies of MoO_x, AuNPs and AuNPs-MoO_x nanocomposites. As shown in Fig. 1A, the typical TEM image shows that blue powder materials are of irregular sheet-like shape nanostructures with large specific surface area, which can provide more attachment sites for AuNPs. AuNPs with a size of about 20 nm are evenly distributed in Fig. 1B. A large amount of AuNPs is uniformly attached to the surface of MoO_x sheets (Fig. 1C), suggesting that the AuNPs-MoO_x nanocomposites have been synthesized successfully. Fig. 1D displays AgNPs with an approximate size of 50 nm are larger than that of AuNPs, which is conducive to signal amplification in subsequent experiments.

X-ray photoelectron spectroscopy (XPS) measurement was performed to further analyze surface chemical formation of MoO_x, AuNPs, AuNPs-MoO_x and AgNPs, as well as the valence and electronic state of metal elements (Mo, Au & Ag). Fig. 1E shows that the full spectra of MoO_x, AuNPs, AuNPs-MoO_x and AgNPs. Compared with MoO_x and AuNPs, the AuNPs-MoO_x composite material contains both Mo and Au elements, suggesting that the AuNPs-MoO_x nanocomposites were successfully synthesized. Moreover, AgNPs that contributed to signal amplification strategy were also peaked at the corresponding position in the full spectrum, which proved the successful synthesis of AgNPs. Besides, the high resolution XPS spectra of Mo, Au and Ag were further analyzed. As shown in Fig. 1F, the valence state of the Mo element in MoO_x (before) and AuNPs-MoO_x (after) is represented and is divided into four peaks including 230.5 eV (Mo^{5+} $3d_{5/2}$), 233.5 eV ($Mo^{5+}3d_{3/2}$), 232.0 eV (Mo^{6+} $3d_{5/2}$) and 234.8 eV (Mo^{6+} $3d_{3/2}$), respectively (Kang et al., 2018; Li et al., 2019; Rajagopal et al., 2011). During the hydrothermal process, the Mo^{VI} precursor (ammonium molybdate) was partially reduced by oleylamine, giving hydrogen molybdenum bronze $H_x(Mo^{V}_x)(Mo^{VI}_{1-x})O_3$ (abbreviated as MoO_x) (Song et al., 2016). The specific reaction equation (1) is as follows:

$$(NH_4)_6Mo^{VI}{}_7O_{24} + HCl \rightarrow H_6Mo^{VI}{}_7O_{24} \xrightarrow[\text{Heat}]{NH_2C_{18}H_{35}} H_x\left(Mo^{V}{}_x\right)\left(Mo^{VI}{}_{1-x}\right)O_3 \quad (1)$$

As shown in Fig. 1G, the peak positions of Au $4f_{7/2}$ and Au $4f_{5/2}$ are about 82.9 eV and 86.6 eV, respectively (Guo et al., 2019; Lv et al., 2018; Li et al., 2016). The two peak positions of Ag $3d_{5/2}$ and Ag $3d_{3/2}$ are assigned to 367.1 eV and 373.1 eV as shown in Fig. 1H (Liu et al., 2018). There were no additional peaks, suggesting that AgNPs was not oxidized during synthesis.

Fig. 2A shows the Raman spectrums of MoO_x, AuNPs and AuNPs-MoO_x. The peaks at 1040, 868 and 663 cm^{-1} in the Raman spectrums of MoO_x and AuNPs-MoO_x could be attributed to the stretching vibration of terminal oxygen (Mo═O), double coordinated bringing oxygen (Mo_2–O) and triple coordinated bringing oxygen (Mo_3–O) groups, respectively.

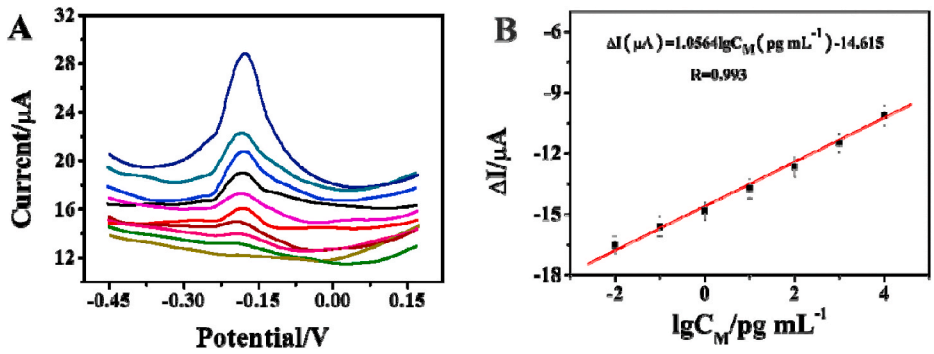

Fig. 3. (A) DPV responses of the designed aptasensor to OTA with different concentrations (0.0, 50000.0, 30000.0, 10000.0, 1000.0, 100.0, 10.0, 1.0, 0.1, 0.01 pg mL^{-1}) in 0.1 M Tris-HCl buffer (pH = 7.42) and (B) the linear relationship between the current increment plotted and the logarithm of concentration of OTA.

Compared with the MoO_3 peaks reported in the literatures (Guo et al., 2019; Huang et al., 2012; Rajagopal et al., 2011; Dieterle and Mestl 2002; Xu et al., 2020), these peaks transferred to a larger wave number, which may be caused by the greater fluidity and less accurate focus of the liquid sample used in the sample measurement. In addition, the individual AuNPs solution also showed its characteristic peak at 958 cm^{-1} (Guo et al., 2019) and it caused certain interference to MoO_x and AuNPs-MoO_x determination because Au has strong fluorescence absorption in this band. Compared to single Raman spectrums of MoO_x and AuNPs, AuNPs-MoO_x contained characteristic peaks of MoO_x and AuNPs, which proved that the composite had been successfully prepared.

Ultraviolet–visible (UV–vis) spectroscopy was used to monitor the process of nanocomposites preparation. MoO_x exhibits a strong and wide absorption peak around at 640 nm and a weak absorption peak at 270 nm (Fig. 2B). The blue color of the nanosheets originates from the intervalence charge-transfer transition between Mo^{V} and Mo^{VI} that coexist in the nanosheets (Guo et al., 2019; Huang et al., 2012). There is a strong and sharp absorption peak at 521 nm, which belongs to the AuNPs characteristic absorption band (Shan et al., 2010; Shu et al., 2017b). For AuNPs-MoO_x nanocomposites, there is not only an absorption peak corresponding to MoO_x at 270 nm, but also a wide absorption band at about 580 nm. Instead of showing absorption peaks of AuNPs and MoO_x at the same time as expected, we hypothesized that the absorption peaks at 580 nm might be a combination of AuNPs and MoO_x absorption peaks. The above results further proved that AuNPs-MoO_x nanocomposites had been successfully prepared. Meanwhile, a characteristic absorption peak around 410 nm is noted for the AgNPs sample due to the surface plasmon resonance effect, indicating the AgNPs sample was successfully synthesized by a simple redox reaction (Zhu et al., 2014; Ma et al., 2009; Lu et al., 2011).

The nanostructure of AuNPs-MoO_x was analyzed using X-ray diffractometer (XRD) as shown in Fig. 2C. The diffraction peaks at 12.266° and 27.258° correspond to the crystalline plane (111) and (231) of Mo_9O_{26}, respectively (JCPDF # 12–0753). The XRD patterns also exhibited two strong peaks at 7.1811° and 9.6900° which are the crystalline planes (200) and (100) of Mo_4O_{11} and MoO_3, respectively (JCPDF # 05–0337) (JCPDF # 21–0569). In addition, the XRD spectrum of AuNPs-MoO_x nanocomposites shows that the diffraction peaks at 38.184°, 44.392° and 64.576° are assigned to the lattice planes (111), (200) and (220) of Au element (JCPDF # 04–0784). Compared with the standard cards of these compounds, the majority of diffraction peaks of the AuNPs-MoO_x nanocomposites can be matched, which proves that the nanocomposites were successfully synthesized.

Electrochemical impedance spectroscopy (EIS, Nyquist plots) was employed to monitor the interfacial property in the aptasensor preparation process, using $[Fe(CN)_6]^{-3/-4}$ as redox probe. Nyquist plots for each surface functionalization step were shown in Fig. 2D. According to Randle theory (Rivas et al., 2015), the electrolytic cell can be simulated to obtain the model circuit as shown in Fig. 2E. In the Nyquist plots, semicircle diameter and straight line corresponds to the charge-transfer resistance (R_{ct}) and warburg impedance (Z_w), respectively. The R_{ct} values are different during each fabrication step. It can be seen that the bare GCE shows a small semicircle (curve a, R_{ct} = 181 Ω), due to high charge-transfer rate constant (k_s). The k_s values of GCE (2.94×10^{-7} cm s^{-1}) is calculated based on the following equation (Vandarkuzhali et al., 2012):

$$R_{ct} = \frac{RT}{n^2F^2k_sC}$$

Here, R represents universal gas constant (8.314 J mol^{-1} K^{-1}), T is temperature (298 K), n is the number of electrons transfer, F is Faraday's constant (96,485 C mol^{-1}), C is the concentration of $[Fe(CN)6]^{3-/4-}$ (5 mM). The R_{ct} value of the bare GCE increased when AuNPs-MoO_x (curve b, R_{ct} = 308 Ω) was dropped. The change of R_{ct} value verified a relatively poor conductivity of MoOx. When walker DNA&5-DNA (curve c, R_{ct} = 610 Ω), MCH (curve d, R_{ct} = 832 Ω), aptamer-OTA&AgNPs (curve e, R_{ct} = 1120 Ω), 1-DNA (curve f, R_{ct} = 1570 Ω) and 2-DNA&3-DNA&4-DNA (curve g, R_{ct} = 1953 Ω) were modified in turn on GCE surface, the R_{ct} value obviously increased due to the negative charge from the phosphate backbone of nucleic acid (Rivas et al., 2015). However, after its interaction with OTA and restriction endonuclease, the partial bases of 5-DNA carrying AgNPs were cut and the R_{ct} value were reduced (curve h, R_{ct} = 1336 Ω). This phenomenon may be ascribed to the reduction of steric hindrance effect. In a nutshell, the changes of EIS demonstrate the success of each modification step.

2.3. Optimization of experimental conditions

To achieve the best performance of the AuNPs- MoO_x based electrochemical aptasensor, several experimental conditions including the mixed concentration of walker DNA&5-DNA, the concentration of AgNPs, reaction time after adding OTA, the volume of restriction endonuclease Nb.BbvCI were investigated. As indicated from Fig. S1A, the peak current value increased first and then decreased gradually with the increasing of the mixed concentration of walker DNA&5-DNA, and the peak current value reached its maximum when the mixture concentration was 1 μM while other conditions remain unchanged. Therefore, 1 μM was selected for sensitive determination of OTA at acceptable throughout. Similarly, we observed that the peak currents changed with the increasing of AgNPs concentrations and a highest signal can be achieved when 0.9 μM of AgNPs was used (Fig. S1B). As depicted in Fig. S1C, the peak current value increased with the prolongation of the reaction time (from 0.5 h to 3 h), and tended to level off after 2 h. Namely, 2 h was selected for optimal reaction time after adding OTA. Besides, the amount of endonuclease Nb.BbvCI also has a great influence on the electrochemical signal. When the dosage of endonuclease Nb. BbvCI was 10 μL, the peak current value reached a stable state

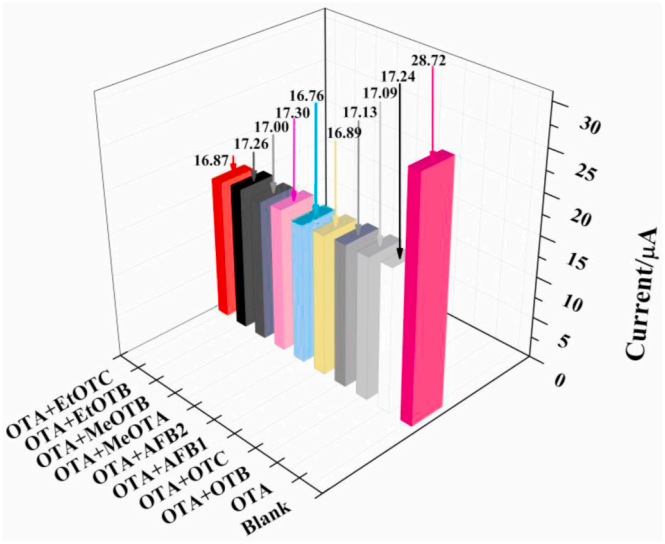

Fig. 4. The specificity of the proposed aptasensor was estimated by DPV in 0.1 M Tris-HCl (pH = 7.42). The concentrations of OTA and other interfering substances were 1000.0 pg mL^{-1}.

(Fig. S1D). Thus, 10 μL was chosen as the optimal volume.

2.4. Study on electrochemical behavior of proposed aptasensor

Under the optimal conditions, DPV was used to determine OTA concentrations. As shown in Fig. 3A, with the concentration increasing, the change degree of peak current increased accordingly. The calibration plot for OTA was illustrated in Fig. 3B. A linear relationship between the △I and logarithm of OTA concentration was obtained with the detection range from 0.01–10000 pg mL^{-1}. The limit of detection (LOD) was 3.3 fg mL^{-1} (S/N = 3), based on 3σ/slope (σ was standard deviation of blank signal, and the slope was obtained from linear fitting equation for low concentration range of OTA) (Wang and Zhao 2020). A comparison of the results of this work with other aptasensors was listed in Table S2, suggesting that the performances of proposed aptasensor were better than that of other reported literatures. Compared with the methods currently published to detect OTA (Mejri-Omrani et al., 2016; Zhu et al., 2018; El-Moghazy et al., 2020; Taghdisi et al., 2021; Wang et al., 2016), our electrochemical aptasensor offers advantages in easy fabrication, simple operation, rapid analysis, high sensitivity, and repeatability. In addition, the fabrication of our sensor is relatively easier without complicated modification steps.

2.5. Selectivity, stability and repeatability of the aptasensor

To estimate the specificity of the proposed aptasensor, different interfering substances, such as OTB, OTC, AFB1, AFB2, and OTA alkyl derivative (MeOTA, MeOTB, EtOTC, EtOTB), were investigated in the supporting electrolyte contained OTA. Compared with pure OTA response, the current value (fluctuating between 16.76 μA and 17.24 μA) generated after adding equal amounts of OTA and interference to the electrolyte could be ignored in Fig. 4. This result confirms that the proposed aptasensor had high selectivity to OTA.

Stability over time and repeatability are key factors in the practical application of sensing systems. The modified electrodes were preserved at 4 °C for 21 days to test storage stability. The proposed aptasensor can remain more than 93.2% of the initial response signal, which was likely a result of partial decomposition or deconjugation of the aptamer on the electrode surface. In addition, six parallel experiments were carried out to detect 1 pg mL^{-1} of OTA to evaluate the repeatability of the designed aptasensor. The relative standard deviation (RSD) of OTA was 3.4%. The result displayed a good repeatability for OTA detection. It should be noted that the modified electrodes allowed detection of a specific concentration of OTA and were not reused, due to the detachment of 5′-DNA from the electrode surface under the action of OTA and exonuclease.

2.6. Real sample analysis

To evaluate the feasibility and reliability of the proposed sensing system for practical applications, the apple juice, orange juice, wine and blood serum were selected as real samples, which could be contaminated with OTA. For real sample analysis, OTA was detected in equal volume of sample solution using a standard spiking method. As shown in Table 1, the recovery for electrochemical sensing spiked samples ranged from 98.47% to 104.3%, with an RSD of less than 4.7%. To further validate the sensor, the detection results were compared with UPLC and the results presented an excellent correspondence. Therefore, these results confirmed that AuNPs-MoO_x nanocomposites could be regarded as applicable electrodes materials for construction of electrochemical aptasensor, and the Nb.BbvCI-aided amplification aptasensor had the potential for OTA sensing in real samples.

3. Conclusion

In a nutshell, we successfully constructed an ingenious and sensitive electrochemical aptasensor for OTA detection based on covalent bonding, hybrid chain reaction and walker DNA machine. Under optimal conditions, the resultant electrochemical aptasensor exhibited an LOD of 3.3 fg mL^{-1} (S/N = 3) and a linear range between 0.01 and 10000 pg mL^{-1} against standard OTA solutions. The electrochemical aptasensor was confirmed the excellent agreement when using a standard spiking method comparing with gold-standard UPLC analysis. Overall, the developed aptasensor allows the detection of OTA with high sensitivity, selectivity, and accuracy in real samples.

CRediT authorship contribution statement

Yahui Wang: Investigation, Methodology, Data curation, Formal analysis, Writing – original draft. **Wei Song:** supplementary experiments; revision; language polishing. **Haiyan Zhao:** revision; discussion, Formal analysis. **Xin Ma:** revision; discussion; language polishing. **Shuying Yang:** revision; discussion, Formal analysis. **Xiujuan Qiao:** revision; discussion, Formal analysis. **Qinglin Sheng:** discussion, Supervision, Investigation, Formal analysis, Validation, Writing – review & editing, Funding acquisition. **Tianli Yue:** discussion, Writing – review & editing, Supervision.

Table 1
Determination of OTA concentration in spiked samples comparing the electrochemical aptasensor with UPLC.

Samples	Measured	Spiked OTA (pg·mL^{-1})	Measured (pg·mL^{-1})		RSD (%)		Recovery (%)	
			this work	UPLC	this work	UPLC	this work	UPLC
apple juice (fresh)	no	10	10.08	10.28	4.70	3.27	100.80	102.80
orange juice (fresh)	no	10	10.03	9.94	2.80	2.22	100.30	99.40
wine	no	10	10.03	10.38	4.20	2.90	100.30	103.80
serum	no	10	10.12	9.87	2.20	1.36	101.20	98.70

Note: the value of Measured (pg·mL^{-1}) is the average of the five times.

Declaration of competing interest

The authors declare that they have no known competing financial interests or personal relationships that could have appeared to influence the work reported in this paper.

Acknowledgments

The authors gratefully acknowledge the financial support of this project by National Key Research and Development Program of China (2019YFC1606703), and the Natural Science Foundation of Shaanxi Province in China (2020JM-429).

Appendix A. Supplementary data

Supplementary data to this article can be found online at https://doi.org/10.1016/j.bios.2021.113171.

References

Chang, Y., Wu, Z., Sun, Q., Zhuo, Y., Chai, Y., Yuan, R., 2019. Anal. Chem. 91 (13), 8123–8128.
Chen, Z.Q., Wang, C., Hao, L.J., Gao, R., Li, F., Liu, S.F., 2019. Biosens. Bioelectron. 128, 104–112.
Dhenadhayalan, N., Yadav, K., Sriram, M.I., Lee, H.L., Lin, K.C., 2017. Nanoscale 9 (33), 12087–12095.
Dieterle, M., Mestl, G., 2002. Phys. Chem. Chem. Phys. 4 (5), 822–826.
El-Moghazy, A.Y., Amaly, N., Istamboulie, G., Nitin, N., Sun, G., 2020. Microchim. Acta 187, 535.
Freitas, A., Barros, S., Brites, C., Barbosa, J., Silva, A.S., 2019. Food Anal. Methods 12, 2675–2684.
Guo, Y., Zhuang, Z., Liu, Z., Fan, W., Zhong, H., Zhang, W., Ni, Y., Guo, Z., 2019. Appl. Surf. Sci. 480, 1162–1170.
Haber, J., Lalik, E., 1997. Catal. Today 33, 119–137.
Hao, L.L., Wang, W., Shen, X.Q., Wang, S.L., Li, Q., An, F.L., Wu, S.J., 2020. J. Agric. Food Chem. 68, 369–375.
Hu, X.K., Qian, Y.T., Song, Z.T., Huang, J.R., Cao, R., Xiao, J.Q., 2012. Chem. Mater. 20 (4), 1527–1533.
Hu, L., Kong, J.M., Han, D.X., Niu, L., Zhang, X.J., 2019. ACS Sens. 4, 235–241.
Huang, Q., Hu, S., Zhuang, J., Wang, X., 2012. Chem. Eur J. 18 (48), 15283–15287.
Kang, Q., Yang, B., Xu, Y., Xu, B., Hou, J., 2018. Adv. Mater. 30 (35), 1801718.
Li, Y., Cain, J.D., Hanson, E.D., Murthy, A.A., Hao, S., Shi, F., Li, Q., Wolverton, C., Chen, X., Dravid, V.P., 2016. Nano Lett. 16 (12), 7696–7702.
Li, Y., Cheng, J., Liu, Y., Liu, P., Cao, W., He, T., Chen, R., Tang, Z., 2017. J. Phys. Chem. C 121 (9), 5208–5214.
Li, Y., Wu, J., Williams, G.R., Niu, S., Zhou, J., Yang, Y., Zhang, X., Fu, Z., Li, D., Zhu, L. M., 2019. ACS Appl. Bio Mater. 2 (10), 4356–4366.
Liu, J.L., Tang, Z.L., Zhang, J.Q., Chai, Y.Q., Zhuo, Y., Yuan, R., 2018. Anal. Chem. 90 (8), 5298–5305.
Lu, W., Liao, F., Luo, Y., Chang, G., Sun, X., 2011. Electrochim. Acta 56 (5), 2295–2298.
Lv, X.H., Li, Y.Y., Yan, T., Pang, X.H., Hu, L.H., Du, B., Wei, Q., 2015. New J. Chem. 39, 4259–4264.
Lv, S., Zhang, K., Zeng, Y., Tang, D., 2018. Anal. Chem. 90 (11), 7086–7093.
Ma, Y.Q., Yi, J.Z., Zhang, L.M., 2009. J. Macromol. Sci., Pure Appl. Chem. 46 (6), 643–648.
Mejri-Omrani, N., Miodek, A., Zribi, B., Marrakchi, M., Hamdi, M., Marty, J.-L., Korri-Youssoufi, H., 2016. Anal. Chim. Acta 92, 37–46.
Quintela, S., Villaran, M.C., Lopez de Armentia, I., Elejalde, E., 2013. Food Contr. 30, 439–445.
Rajagopal, S., Nataraj, D., Khyzhun, O.Y., Djaoued, Y., Robichaud, J., Senthil, K., Mangalaraj, D., 2011. CrystEngComm 13 (7), 2358–2368.
Rivas, L., Mayorga-Martinez, C.C., Quesada-Gonzalez, D., Zamora-Galvez, A., de la Escosura-Muniz, A., Merkoci, A., 2015. Anal. Chem. 87, 5167–5172.
Sari, F.N.I., Ting, J.M., 2018. ChemSusChem 11 (5), 897–906.
Shan, C., Yang, H., Han, D., Zhang, Q., Ivaska, A., Niu, L., 2010. Biosens. Bioelectron. 25 (5), 1070–1074.
Shu, B., Zhang, C., Xing, D., 2017a. Biosens. Bioelectron. 97, 360–368.
Shen, Y., Gong, J.M., Li, S.Q., Liu, C.Y., Zhou, L.L., Sheng, J.H., Xu, Q.X., 2021. Sens. Actuators, B 329, 129078.
Shu, Y., Chen, J., Xu, Q., Wei, Z., Liu, F., Lu, R., Xu, S., Hu, X., 2017b. J. Mater. Chem. B 5 (7), 1446–1453.
Song, G., Hao, J., Liang, C., Liu, T., Gao, M., Cheng, L., Hu, J., Liu, Z., 2016. Angew. Chem., Int. Ed. Engl. 55 (6), 2122–2126.
Taghdisi, S.M., Danesh, N.M., Ramezani, M., Alibolandi, M., Nameghi, M.A., Gerayelou, G., Abnous, K., 2021. Talanta 223, 121705.
Tao, F., Fang, J., Guo, Y., Tao, Y., Han, X., Hu, Y., Wang, J., Li, L., Jian, Y., Xie, G., 2018. Anal. Biochem. 554, 16–22.
Vandarkuzhali, S., Gogoi, N., Ghosh, S., Reddy, B.P., Nagarajan, K., 2012. Electrochim. Acta 59, 245.
Veerapandian, M., Avti, P.K., Ravichandiran, V., 2017. Colloids Surf., B 154, 315–320.
Wang, C., Zhao, Q., 2020. Biosens. Bioelectron. 167, 112478.
Wang, B., Wu, Y.Y., Chen, Y.F., Weng, B., Xu, L.Q., Li, C.M., 2016. Biosens. Bioelectron. 81, 125–130.
Wang, K., He, M.Q., Zhai, F.H., Wang, J., He, R.H., Yu, Y.L., 2018. Biosens. Bioelectron. 105, 159–165.
Wei, M., Wang, C., Xu, E., Chen, J., Xu, X., Wei, W., Liu, S., 2019. Food Chem. 282, 141–146.
Xu, Y.M., Zheng, W.B., Hu, Y.M., Tang, C., Jia, A.P., Lu, J.Q., 2020. J. Catal. 381, 222–233.
Yan, J.X., Hu, W.J., You, K.H., Ma, Z.-e., Xu, Y., Li, Y.P., He, Q.H., 2020. J. Agric. Food Chem. 68 (7), 2193–2200.
Yang, F., Zhong, X., Jiang, X., Zhuo, Y., Yuan, R., Wei, S., 2019. Biosens. Bioelectron. 130, 262–268.
Yao, B., Huang, L., Zhang, J., Gao, X., Wu, J.B., Cheng, Y.L., Xiao, X., Wang, B., Li, Y., Zhou, J., 2016. Adv. Mater. 28, 6353–6358.
Yin, W., Bao, T., Zhang, X., Gao, Q., Yu, J., Dong, X., Yan, L., Gu, Z., Zhao, Y., 2018. Nanoscale 10 (3), 1517–1531.
Zhan, Y., Liu, Y., Zu, H., Guo, Y., Wu, S., Yang, H., Liu, Z., Lei, B., Zhuang, J., Zhang, X., Huang, D., Hu, C., 2018. Nanoscale 10 (13), 5997–6004.
Zhang, T., Xing, B., Han, Q., Lei, Y., Wu, D., Ren, X., Wei, Q., 2018. Anal. Chim. Acta 1032, 114–121.
Zhang, T.Y., Sun, X.F., Li, L., Ma, J.M., Zhang, R.Q., Liu, X.L., Li, N., Dyce, P.W., Shen, W., 2019. J. Agric. Food Chem. 67 (9), 2679–2690.
Zhang, X.Y., Wu, T.T., Yang, Y.M., Wen, Y.Q., Wang, S.T., Xu, L.-P., 2020. Sens. Actuators, B 321, 128472.
Zhou, J., Deng, S.Z., Xu, N.S., Chen, J., She, J.C., 2003. Appl. Phys. Lett. 83, 2653–2655.
Zhu, J., Kim, K., Liu, Z., Feng, H., Hou, S., 2014. Electroanalysis 26 (11), 2513–2519.
Zhu, X., Kou, F.X., Xu, H.F., Han, Y.J., Yang, G.D., Huang, X.J., Chen, Y.W., Lin, Z.Y., 2018. Sens. Actuators, B 70, 263–269.